




Construction of amorphous carbon-coated α -Fe₂O₃ core–shell nanostructure for efficient photocatalytic performance

Jianle Xu^{1,2,3,*} , Qing Yao¹, Pengwei Li¹, Xiao Zhang², Shuang Wang^{2,*}, and Chunxu Pan^{3,*}

¹ College of Information and Computer, Center of Nano Energy and Devices, Taiyuan University of Technology, Taiyuan 030024, People's Republic of China

² College Environmental Science & Engineering, Taiyuan University of Technology, Taiyuan 030024, People's Republic of China

³ School of Physical Science and Technology, Wuhan University, Wuhan 430072, People's Republic of China

Received: 25 July 2022

Accepted: 30 August 2022

Published online:

13 September 2022

© The Author(s), under exclusive licence to Springer Science+Business Media, LLC, part of Springer Nature 2022

ABSTRACT

Hetero-structured semiconductor composite as an ideal multifunctional photocatalyst has significant advantage for the improvement of photocatalytic efficiency. Here, core–shell hetero-structured α -Fe₂O₃@Carbon (α -Fe₂O₃@C) composite including of α -Fe₂O₃ nanoparticles (NPs) inner-core and amorphous carbon outer-shell was successfully synthesized via a simple hydrothermal method. The experiment results indicate that the present core–shell structure has a remarkable impact on the interfacial synergies. The possible photocatalytic mechanism of core–shell α -Fe₂O₃@C composite is investigated in detail. Thanks to the following advantages: the core–shell structure provides more heterogeneous interfaces, so the incident light would be reflected multiply and enhanced the light absorption capacity. In addition, the heterogeneous interface synergistic effect between amorphous carbon and α -Fe₂O₃ as the bridge gives rise to a rapid approach to transport photo-induced carriers and thus enhances the electronic transfer capacity. It is anticipated that the core–shell nanostructure provides a neoteric mentality for designing superior photocatalysts with outstanding advantageous features applicable to, among others, hydrogen generation, green energy, water splitting, etc.

1 Introduction

Nowadays, water purification and reuse have been proved to be an easy or eco-friendly fix to moderate shortages of clean water caused by excessive use of

pesticides, organic dyes, detergents, [1, 2] et al. Photocatalysis technologies based on semiconductor oxides have become an optional and effective approach to reducing environmental pollution and efficient utilization of green energy [3–6]. It is well

Address correspondence to E-mail: xujianle@whu.edu.cn; wangshuang@tyut.edu.cn; cxpan@whu.edu.cn

known that the typical photocatalytic reaction can be succeeded along with the generation of electrons in the conduction band (CB) and holes in the VB (valence band) under visible irradiation [7, 8]. Furthermore, the activity of photocatalytic reaction is influenced by the light intensity, intrinsic energy gap, absorption edge and surface structure including defects, surface area of photocatalyst [9–12]. One of the foremost mechanisms is the activity of photoelectrons can affect the reaction efficiency [13, 14]. However, the high recombination rate of photoelectrons and holes of single semiconductor oxides limits the photocatalytic performance and leads to low photocatalytic efficiency [15, 16]. Numerous strategies have been explored to enhance the photocatalytic activity such as reducing the recombination rate by forming heterojunction, optimization in conductivity by doping with conductive material for expediting the electronic transfer capacity [17–19]. Compared to the single photocatalyst, core–shell hetero-structured semiconductor oxide composite photocatalyst in which semiconductor oxides acts as the core and conductive material acts as the shell has attracted extensive consideration due to their unique performances with salient advantageous features such as electronic transfer capacity and photoelectric synergistic effect [20, 21].

In this context, α -Fe₂O₃ as an environmentally and friendly n-type semiconductor has been considered as one of promising candidates for photocatalytic applications, drug delivery platform and bio-chemical sensors which due to its narrow energy gap and excellent chemical stability [22–25]. However, improving the photocatalytic efficiency of α -Fe₂O₃ to fulfill practical application remains an enormous challenge, because of low diffusion length and high electron–hole pairs recombination led to the bottleneck of poor quantum yield and visible-light trapping [26]. One of the keys to overcome these conditions is lowering the recombination rate by forming core–shell hetero-structure, enhancement in conductivity by combining with carbonaceous material for improving the charge transfer ability [27]. Inspired by this observation, among the most correlational research of α -Fe₂O₃ the main focus appears to construct α -Fe₂O₃-based hetero-structured materials in different forms. Constructing a core–shell structure, which is designed based on α -Fe₂O₃ core and carbonaceous materials shell, is an intentional approach to optimize the excellence of the interface

synergistic effect. Moreover, this core–shell hetero-structured designing mentality would minimize the electron and hole spatial overlap [21]. The combination approach of core–shell heterojunction solves the low diffusion length and decreases the electron–hole recombination, and expedites the electron transfer while enhancing photocatalytic performance and stability.

In this work, we report a sample and effective strategy to solve the aforementioned bottleneck of single α -Fe₂O₃ in the photocatalytic field. The core–shell structure of amorphous carbon-encapsulated α -Fe₂O₃ composite was synthesized via a one-step hydrothermal method. The experiments prove that this core–shell structured α -Fe₂O₃@C nanocomposite is the superior photocatalyst for photocatalytic degradation of rhodamine B (RhB). The possible photocatalytic mechanism of as-synthesized α -Fe₂O₃@C composite was investigated in detail. The interface synergistic effects of core–shell structure between amorphous carbon and α -Fe₂O₃ are likely to enhance the electronic transfer capacity and the photocatalytic activity. Our findings provide a neoteric mentality for designing a novel photocatalyst and enrich a potential application in the photoelectric energy conversion.

2 Experimental

2.1 Synthesis of the α -Fe₂O₃ NPs precursor

The α -Fe₂O₃ NPs precursor were synthesized via a simple hydrothermal method. In the specific experimental process: 0.6 g of ferric chloride and 1 g of sodium acetate were dissolved in 120 mL of deionized water. And the mixed solution was stirred until dissolved to form a stable solution. After dissolving completely, the stirred suspension was poured into an autoclave with a capacity of 120 mL and heated at 250 °C for 5 h. After the completion of the reaction and allowed cool to room temperature. Finally, the reaction products were centrifuged and separated from the black precipitation with deionized water and anhydrous ethanol.

2.2 Generation of core–shell structured α - Fe_2O_3 @C nanocomposite

0.25 g of the as-prepared α - Fe_2O_3 NPs was dispersed in 60 mL of ethanol solution. Then, 0.26 g ferric chloride and 0.16 g terephthalic acid were added to the above-mentioned ethanol solution and the dispersion was uniform by ultrasonic for 10 min. The mixed solution was poured into a beaker and stirred in a water bath at 70 °C for 30 min. The precipitates were separated by centrifugation and washed with deionized water and anhydrous ethanol, respectively. 0.12 g of mentioned above α - Fe_2O_3 dispersed into 50 mL of deionized water, and glucose ($\text{C}_6\text{H}_{12}\text{O}_6 \cdot \text{H}_2\text{O}$, 0.1 mol, 0.2 mol, 0.3 mol) with different mole ratios of α - Fe_2O_3 were added into the mixed solution. After uniform ultrasonic dispersion, the products were transferred to autoclave with a capacity and heated at 220 °C for 12 h. The precipitate was separated by centrifugation and washed three times with deionized water and anhydrous ethanol. The products generated with different mole ratios glucose (0.1 mol, 0.2 mol, 0.3 mol) were denoted hereinafter as S1, S2 and S3, respectively.

2.3 Characterization techniques

The structural characterization of samples was characterized by the X-ray diffraction (XRD) configuration using a powder diffractometer (Bruker AXS, Karlsruhe, Germany). The morphology and micro-structural of as-prepared samples were examined using scanning electron microscopy (SEM, JSM-7001F, JEOL, Japan) and transmission electron microscopy (TEM, 2100F; JEOL, Japan), separately. UV–VIS spectra were tested by the spectrophotometer (3100 UV–VIS–NIR, Shimadzu, Kyoto, Japan). The Raman spectrum was recorded by a spectrometer (Raman-11, Nanophoton Corporation, Japan) at room temperature.

2.4 Photoelectrochemical measurements and photocatalytic activity

The photoelectrochemical (PEC) is tested via using an electrochemical workstation (IM6, Zahner, Karlsruhe, Germany) and the 500 W Xe light was used as the source of visible light. First, 1 mg as-prepared samples were mixed with 10 mL Nafion and 10 mL ethanol, the mixed was smeared on 1 cm² square FTO

glass and then the samples were dried at 60 °C for 3 h in air. The above dried glass was used as the working electrode, Ag/AgCl electrode and a Pt wire were employed as the reference electrodes and counter, respectively. Then, Na_2SO_4 solution (0.2 mol/L) was employed as the electrolyte. The photocurrent property of the photoanode was carried out in each 60 s respectively.

The concentration variation of RhB solution was displayed from the spectrum strength of the absorption for the UV–Vis light irradiation. 100 mL of the RhB solution, with an initial concentration of 10 mg/L was deposited in a container. The mixed liquor was stirred in a dark environment for 10 min to ensure equilibrium of adsorption desorption. The maximum absorbance of extracting solution was analyzed by the spectrophotometer, while the variations of the absorption maximum at different intervals was tested. The concentration of RhB aqueous was decided by measuring intensity of the maximum absorbance wavelength of the suspension liquid. The degradation percentage (η) of the solutions could be calculated by follows [28]:

$$\eta = \frac{C_0 - C_t}{C_0} \times 100$$

The rate of dye degradation is quantified with the first order exponential fit. Where the C_0 is the initial RhB dye concentration, C_t the dye concentration after an illumination time t (min). The variation of the RhB relative concentrations (C_t/C_0 , and $-\ln(C_t/C_0)$) as a function of irradiation time.

3 Results and discussions

The morphology and micro-structure of α - Fe_2O_3 and the as-prepared α - Fe_2O_3 @C samples (S1–S3) were conducted through SEM and TEM. As shown in Fig. 1a, α - Fe_2O_3 has a spherical shape with a uniform diameter of around 20 nm, and the appearance of the single α - Fe_2O_3 consists in the state of particle aggregation. The results show that with the increase of content of glucose, the diameter of α - Fe_2O_3 @C sample was increased. When the α - Fe_2O_3 @C sample generated with the mole ratios of glucose of 0.2 mol and 0.3 mol, and that leads to the aggregation performance degradation of α - Fe_2O_3 @C nanocomposites. This is mainly due to the small pore size of amorphous carbon material, and the carbon shell

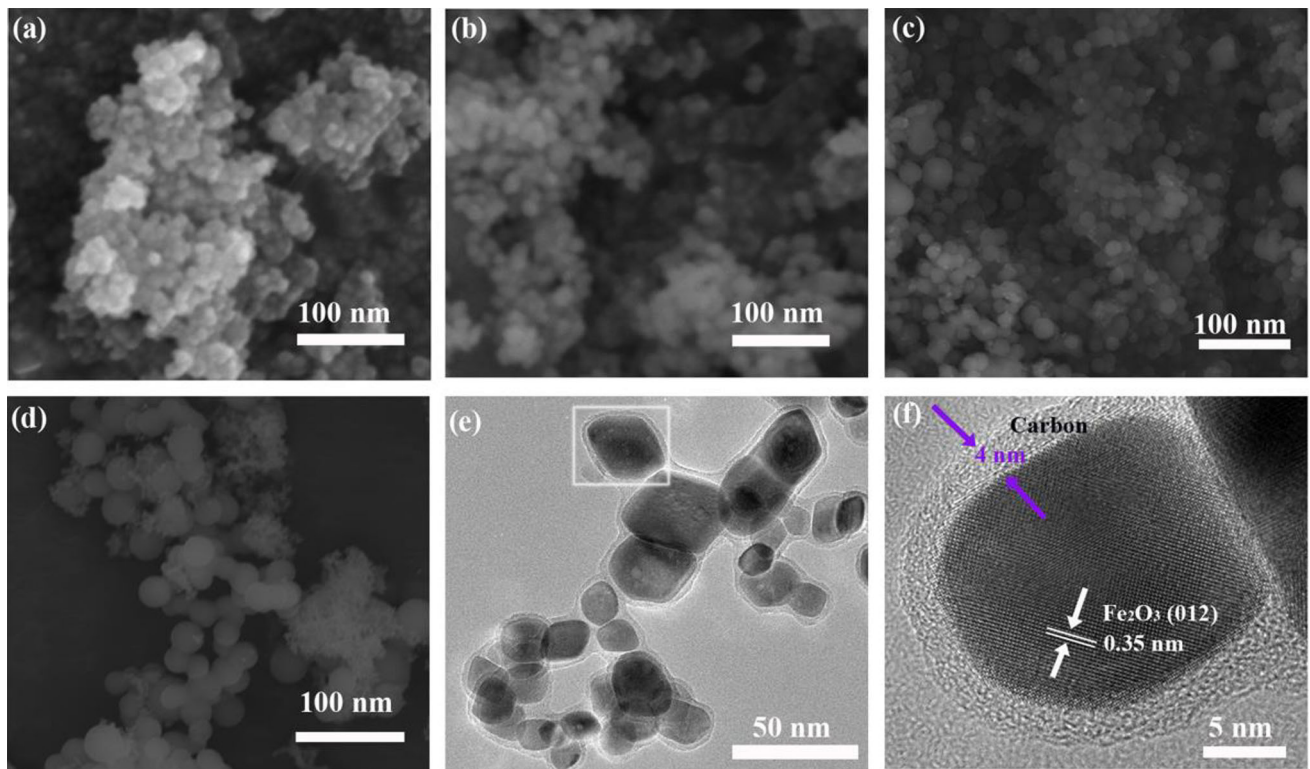


Fig. 1 SEM images of α -Fe₂O₃ NPs (a), α -Fe₂O₃@C S1-S3 (b–d), TEM and HRTEM images of α -Fe₂O₃@C S2 (e–f)

inhibits the agglomeration of α -Fe₂O₃@C NPs [29, 30]. In order to investigate the specific micro-structure of α -Fe₂O₃@C NPs, the TEM and HRTEM images of S2 (as shown in Fig. 1e, f) prove that core–shell like structure composites with obvious contrast between the black and gray parts can be observed, demonstrating that the shell is amorphous carbon material. As displayed in Fig. 1f, the HRTEM of α -Fe₂O₃@C S2 indicates the changes in diameter were from 20 nm for core spheres to 24 nm for core–shell composite. It can be proved that the amorphous carbon is successfully coated on the surface of α -Fe₂O₃ NPs with the thicknesses of about 4 nm. The HRTEM also shows lattice spacing of core is about 0.35 nm, which corresponds to the (012) plane of α -Fe₂O₃. It can also find that the outer carbon shell exhibits amorphous nature. Based on the above results, the as-prepared α -Fe₂O₃@C nanocomposites are the core shell structure with α -Fe₂O₃ NPs packaged with amorphous carbon, obviously.

Figure 2 displays the XRD patterns and Raman spectra of α -Fe₂O₃ and as-prepared α -Fe₂O₃@C samples (S1-S3). It can be found that the XRD patterns centered at 24.14°, 33.14°, 35.62°, 40.84°, 49.46°, 54.04°, 57.56°, 62.44°, 63.95°, 71.85° and 75.39° are

assigned as (012), (104), (110), (113), (024), (116), (018), (214), (300), (101) and (200) crystal planes of typical rhombohedral α -Fe₂O₃ (JCPDS card No. 33-0664), respectively. Moreover, the diffraction peaks of both α -Fe₂O₃@C samples (S1-S3) are indexed by the rhombohedral α -Fe₂O₃ phase without any obvious peaks of other phases. Dramatically, no distinct diffraction peaks of amorphous carbon phase are observed in the α -Fe₂O₃@C nanocomposites. The peaks corresponding to amorphous carbon could be

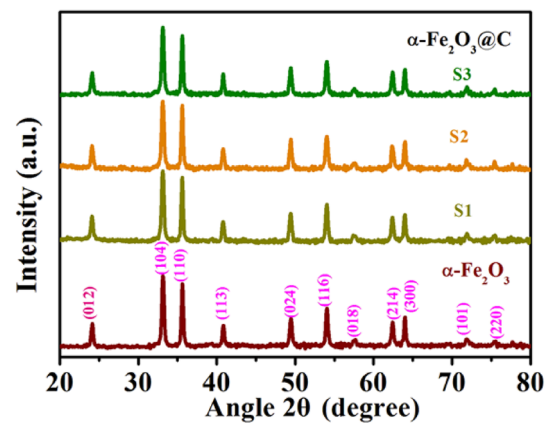


Fig. 2 XRD patterns of α -Fe₂O₃ NPs and α -Fe₂O₃@C S1-S3

too weak to be clearly observed [31]. Researchers were able to use Raman spectroscopy to look at the change of the vibrational energy of the bond and then characterize the variety rules of the structure of carbon materials [32, 33].

Figure 3 illustrates the Raman spectra of α -Fe₂O₃ and α -Fe₂O₃@C samples (S1-S3). Obviously, it can find that the different typical Raman spectrum of as-prepared α -Fe₂O₃@C samples S1-S3. The peaks corresponding to samples (S1-S3) at around 1341 cm⁻¹ and 1595 cm⁻¹ corresponds to the D band and G band, respectively. It can see that the D band and G band relate to the disorder induced in the carbon structure and the vibration of sp² carbon vibration, respectively. On the contrary, no characteristic peaks of carbon were detected in α -Fe₂O₃. The Raman results indicate amorphization of graphite including more topological defects, disorders and vacancies in the carbon shell of the α -Fe₂O₃@C sample [34]. On the basis of above analysis, the α -Fe₂O₃@C nanocomposite with core-shell structure is an ordered assembly system in which α -Fe₂O₃ NPs are covered with carbon materials via chemical bonds or other interactions [35], and the outer carbon shell also retained amorphous nature.

Photocurrent measurement normally is used for inquiring the separation efficiency of photo-induced carriers (electrons or holes) [36, 37]. Photocurrents of the as-prepared single α -Fe₂O₃ and α -Fe₂O₃@C samples (S1-S3) were gauged for studying the electronic interaction between α -Fe₂O₃ and carbon materials, and the current density versus potential curves were recorded via circularly turn on and off the light irradiation, as shown in Fig. 4. Dramatically, all α -Fe₂O₃@C samples exhibit higher transient

photocurrent when compared with single α -Fe₂O₃, and the photocurrent of the α -Fe₂O₃@C S2 reached 0.25 mA/cm² and was about two times as high as that of single α -Fe₂O₃. It evidences that the core-shell complex structure could effectively restrain current carrier recombination. Moreover, outer shell carbon as a protective material could inhibits the photo-corrosion of α -Fe₂O₃ under visible-light illumination. In addition, it can be found that the transient photocurrent value of α -Fe₂O₃@C displays a rising and falling variation trend, which meant that the additive amount of glucose in α -Fe₂O₃@C samples is closely related to surface carrier concentration. Notably, compared to the other samples, the α -Fe₂O₃@C S2 also presents higher photocurrents owing to optimal additive amount of glucose or the layer thickness of outer carbon shell. Here, the core-shell structure offers a large interface between the α -Fe₂O₃ core and the carbon shell. The core-shell structure contains many heterojunction interfaces and the surface states raised by the larger core-shell interface [38]. It creates the good possibility for leaping into the conduction band edge [39]. Thus, the balance of synergistic and the charge separation leads to enhanced transient photocurrent efficiency.

In order to study the photo absorption ability and optical properties of as-prepared α -Fe₂O₃ and α -Fe₂O₃@C, Fig. 5 illustrates the light absorption of pure α -Fe₂O₃ and α -Fe₂O₃@C S2 nanocomposite. The absorption peak of α -Fe₂O₃@C S2 is 460 nm, which is similar to the single α -Fe₂O₃ except for about 15 nm red shift. The construction of α -Fe₂O₃@C core-shell structure may leads to a red-shift, which is conducive to the light utilization and photoelectric conversion efficiency [40]. This phenomenon could be

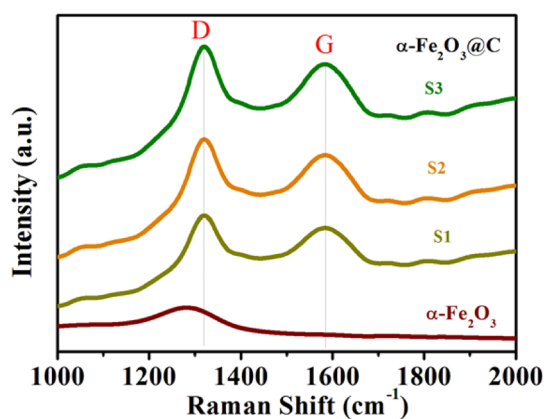


Fig. 3 Raman spectra of α -Fe₂O₃ NPs and α -Fe₂O₃@C S1-S3

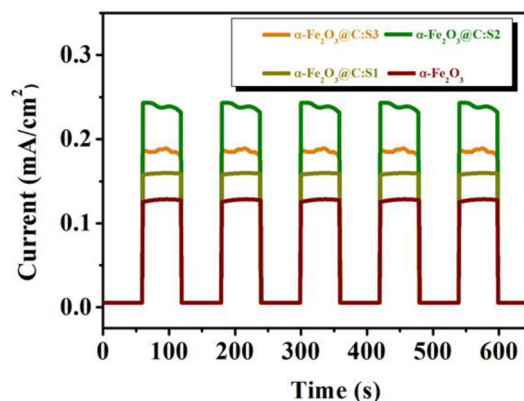


Fig. 4 Photocurrent density of α -Fe₂O₃ NPs and α -Fe₂O₃@C S1-S3 under visible light on-off cycles

attributed to the following reasons: the synergistic effect for light absorption was generated in the α -Fe₂O₃@C core-shell structure. In other words, when a large interface contact area existed between carbon materials and α -Fe₂O₃ NPs, the interfacial scattering effect of visible light was enhanced. As a result, the transmission of the visible photon in the α -Fe₂O₃@C nanocomposite was increased via longer optical path length [41], which led to a significantly enhanced light absorption in the visible region. Meanwhile, these interface and surface states of the α -Fe₂O₃@C core-shell structure accompanied with carbon defect states would result in the composites obvious to the visible light [42]. The results indicate that α -Fe₂O₃@C exhibits a semiconductor character with an indirect band gap. Band-gap energies (E_g) are evaluated from the absorption edges of the reflectance spectra, as shown in the insets of Fig. 5. It is observed that band gap of α -Fe₂O₃@C (2.25 eV) is smaller than that of α -Fe₂O₃ (2.36 eV). The observed narrowing of the band gap in α -Fe₂O₃@C nanocomposite can be considered to be attributable to the increased hybridization of the energy levels by the surface defects formed of amorphous carbon materials, shifting the valence and conduction bands and subsequently decreasing the band gap [43]. It can also be considered to attributable to oxygen vacancies leading to lowered about 0.11 eV. Therefore, the core-shell heterojunction of α -Fe₂O₃@C boosted the separation and utilization of photo-induced carriers and improved the photocatalytic performance [44].

To study the photocatalytic activity of as-prepared α -Fe₂O₃ and α -Fe₂O₃@C NPs, the degradation experiment for RhB solution was carried out as

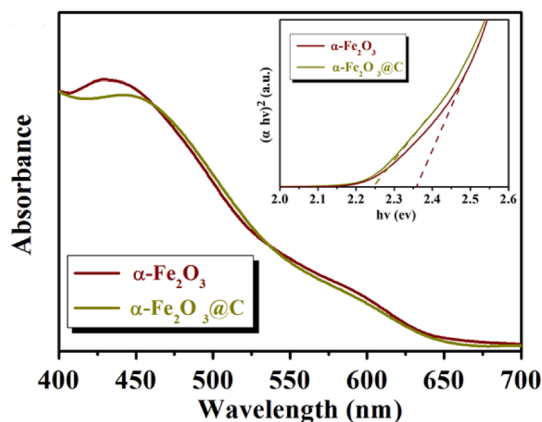


Fig. 5 UV–VIS absorption spectra for α -Fe₂O₃ NPs and α -Fe₂O₃@C S2

shown in Fig. 6. For comparison, the control experiment was carried out under in dark environment and without photocatalyst under the UV–vis light irradiation, respectively. As shown in Fig. 6a, it can be found that RhB reaches the adsorption desorption equilibrium under dark conditions within 10 min. In the absence of photocatalyst, there is no appreciable degradation of RhB, significantly. The degradation curves of RhB under the UV–vis light irradiation are shown in Fig. 6b. It can be found that crystal core-amorphous shell structured α -Fe₂O₃@C samples exhibit excellent photocatalytic degradation performance, leading to the significant improved performance compared to pure α -Fe₂O₃. After 80 min of reaction, the degradation of RhB rates reach 38%, 81%, 99.8% and 67% for α -Fe₂O₃ and α -Fe₂O₃@C (S1–S3), respectively. Obviously, the photocatalytic performance of the α -Fe₂O₃@C S2 nanocomposite is the most optimal. The experimental results are similar to that of photocurrent measurement.

According to Fig. 7a, the photocatalytic activity of α -Fe₂O₃@C is much higher than that of single α -Fe₂O₃, and the distinct rate constant (k , min⁻¹) of α -Fe₂O₃@C S2 reaches the maximum of 0.024 min⁻¹. Notably, the order of rate constant is S2 > S1 > S3 > α -Fe₂O₃. Moreover, the degradation stability performance is also a key factor for the α -Fe₂O₃@C. The degradation curves of RhB for three cycles is shown in Fig. 7b, it can be seen that the photocatalytic performance of the α -Fe₂O₃@C S2 nanocomposite remained almost unchanged. The circulation experiments proved that core-shell α -Fe₂O₃@C structure provide a pathway to have the most efficient photocatalytic stability and reproducibility. The photocatalytic performances of as-prepared samples were evaluated by the degradation of different kinds of dyes Phenol, Methylbenzene (MB), Methyl Orange (MO), and Congo Red (CR) as shown in Fig. 7c. Moreover, compared with several common core-shell photocatalysts for 80 min degradation of RhB as shown in Table 1, it's obvious to observe that α -Fe₂O₃@C has an excellent photocatalytic performance in the cationic dyes. From Fig. 7d, the signals of DMPO•OH were readily detected with the α -Fe₂O₃ and α -Fe₂O₃@C system, confirming the formation of •OH radicals.

Based on the above analysis, the schematic diagram of proposed photocatalytic mechanism of α -Fe₂O₃@C nanocomposite is illustrated in Fig. 8. First, the core-shell structured composite formed when

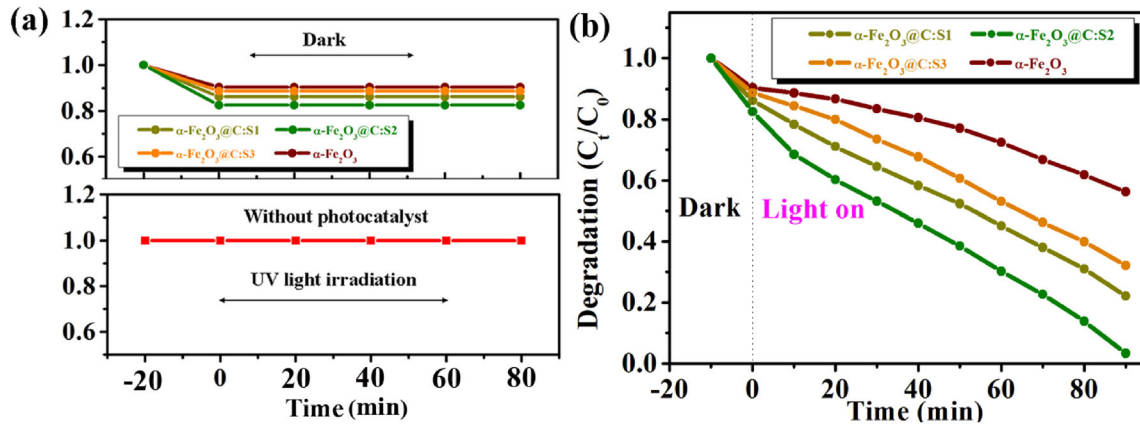


Fig. 6 Degradation profiles of RhB in the presence of photocatalysts in dark and in the absence of photocatalysts with light irradiation (a), degradation profiles of RhB photocatalytic degradation (b)

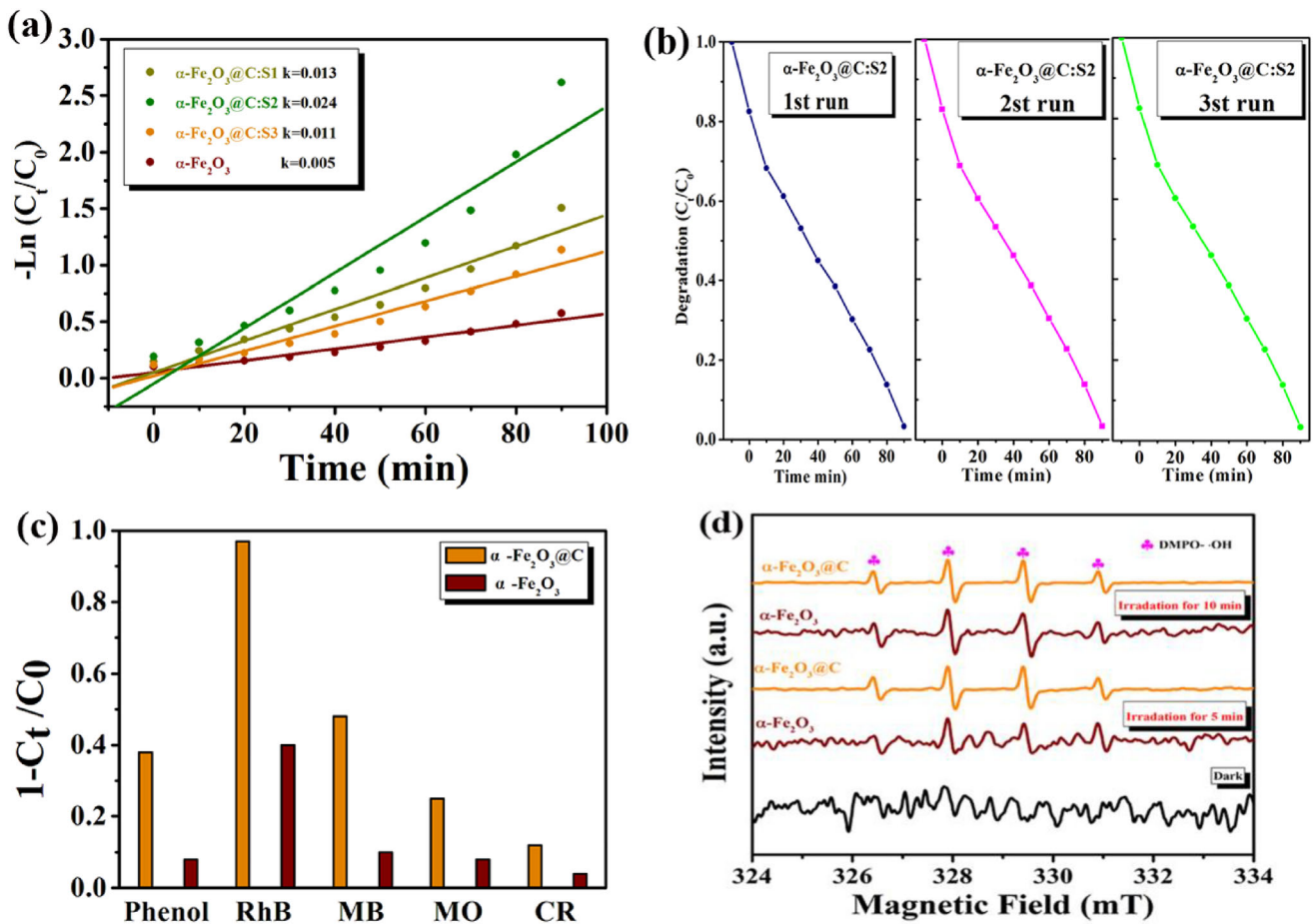


Fig. 7 Kinetic curves of the RhB degradation (a), photocatalytic activity of the $\text{Fe}_2\text{O}_3\text{@C}$ S2 for RhB degradation with three times cycling (b). Photocatalytic degradation of several different

pollutants with prepared photocatalysts (c). ESR spectra in the $\alpha\text{-Fe}_2\text{O}_3$ and $\alpha\text{-Fe}_2\text{O}_3\text{@C}$ system with DMPO- $\bullet\text{OH}$ (d)

amorphous carbon materials are coated on the surface of $\alpha\text{-Fe}_2\text{O}_3$ NPs. Under irradiation, more pathways provided a faster interfacial charge carrier

transfer attributed to reasonable core–shell structure [48, 49]. Second, when the $\alpha\text{-Fe}_2\text{O}_3$ absorbs energy to produce photogenerated electron–hole pair, the free

Table 1 Comparison of several common core–shell photocatalysts for 80 min degradation of RhB

Catalyst	Amount (mg)	Degradation (%)	$K_{app}/(\text{min}^{-1})$	$K_{nor}/(\text{min}^{-1}.\text{mg})$	Reference
TiO ₂ @C	50	80	0.021	4.2×10^{-4}	[45]
ZnFe ₂ O ₄ @C	0.05	24.4	7.26×10^{-4}	0.0146	[46]
α -Fe ₂ O ₃ @TiO ₂	40	73	0.0145	3.6×10^{-4}	[47]
α -Fe ₂ O ₃ @SnO ₂	10	56.08	0.0069	6.9×10^{-4}	[48]
α -Fe ₂ O ₃ @SnO ₂ @Cu ₂ O	10	78.76	0.0228	2.2×10^{-3}	[48]
α -Fe ₂ O ₃ @C-S1	10	81	0.013	1.3×10^{-3}	This work
α -Fe ₂ O ₃ @C-S2	10	99.8	0.024	2.4×10^{-3}	This work
α -Fe ₂ O ₃ @C-S3	10	67	0.011	1.1×10^{-3}	This work

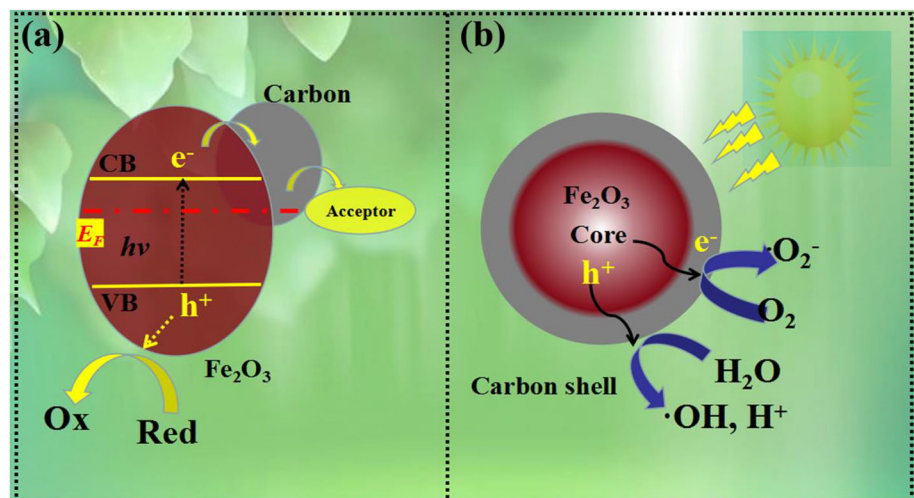
electrons are excited from the VB of α -Fe₂O₃ into its conduction band in a specific photocatalytic reaction (see Fig. 8a). The interface transfer process contains holes and excited electrons and its deactivation by recombination, identifies the efficiency of the photocatalyst [50, 51]. In particular, the excited electrons can transfer from α -Fe₂O₃ to carbon materials through the interface between core–shell structure more easily. Thus, both processes make for electron separation and stabilization, hindering the electron hole pair recombination process (Fig. 8b). In the end, the electron–hole pairs are divided effectively, the holes are trapped by H₂O to form hydroxyl radicals ($\cdot\text{OH}$). And the reserved electrons in the CB of α -Fe₂O₃ reacted with O₂ to produce radical dot $\cdot\text{O}_2^-$, which was involved in the degradation of organic substrates [52]. Thus, the electrons transferred in CB can reduce the absorbed O₂ to create active $\cdot\text{O}_2^-$ [53]. And so beyond that, the produced $\cdot\text{O}_2^-$ liveness are not only can degrade pollutants, but also a provenience of $\cdot\text{OH}$ radicals and photodegradation rate is

perfected. As a consequence, the more radical $\cdot\text{OH}$ radical and remaining active $\cdot\text{O}_2^-$ are assigned to the photodegradation of RhB pollutants rapidly [54, 55]. Therefore, the core–shell heterojunction of α -Fe₂O₃@C boosted the separation and utilization of photo-induced carriers and improved the photocatalytic performance [56, 57].

4 Conclusions

To make full use of the interfacial synergies and separation efficiency of electron–hole pair, a strategy of core–shell structure designing is proposed to effectively enhance the photocatalytic property. By regulating and controlling the content of carbon, the core–shell structured α -Fe₂O₃@C composite including of inner-core α -Fe₂O₃ NPs and outer-shell amorphous carbon is successfully prepared via a simple hydrothermal method. Compared with the pure α -Fe₂O₃, it can be proved that the as-prepared α -

Fig. 8 Schematic for the energy band structure and proposed photodegradation mechanism of α -Fe₂O₃@C



Fe₂O₃@C nanocomposite exhibits improved and effective photocatalytic activity for the degradation of RhB. Owing to the core–shell structure endowing more pathways for the charge carrier transfer and the interfacial synergies mechanism. As a result, the photogenerated electron–hole pairs are separated effectively between the core–shell interface, and the efficient separation of electron and hole is the primary motivation for enhancement of the photocatalytic performance. This study provides a neoteric mentality for the fabrication of novel hetero-structure for photocatalysis or other green energy applications.

Acknowledgements

This work was supported by the Special Talents in Shanxi Province (Grant No. 201901D211074), National Natural Science Foundation of China (Grant No. 21671147)

Author contributions

JX contributed to conception and experiment design. JX and QY contributed to experiment operation, acquisition of data, analysis, and interpretation of data. PL and SW contributed to acquisition of data and drafting the article. JX and XZ contributed to revising article critically for important intellectual content. JX contributed to analysis and interpretation of data. CP contributed to experiment design.

Funding

Special Talents in Shanxi Province, 201901D211074, Jianle Xu, National Natural Science Foundation of China, 21671147, Shuang Wang

Data availability

All data generated or analyzed during this study are included in this published article.

Declarations

Conflict of interest All authors declare no conflict of interest.

Research involving human and animal participants This article does not contain any studies with human participants or animals performed by any of the authors. In this experiment, we did not collect any samples of human and animals.

References

1. X. Liu et al., Noble metal-metal oxide nanohybrids with tailored nanostructures for efficient solar energy conversion, photocatalysis and environmental remediation. *Energy Environ Sci.* **10**, 402–434 (2017)
2. V.J. Babu et al., Review of one-dimensional and two-dimensional nanostructured materials for hydrogen generation. *Phys. Chem. Chem. Phys.* **17**, 2960–2986 (2015)
3. A. Fujishima, K. Honda, Electrochemical photolysis of water at a semiconductor electrode. *Nature* **238**(5358), 37–38 (1972)
4. X. Chen et al., Semiconductor-based photocatalytic hydrogen generation. *Chem. Rev.* **110**(11), 6503–6570 (2010)
5. M.Q. Wen et al., Synthesis of MoS₂/g-C₃N₄ nanocomposites with enhanced visible-light photocatalytic activity for the removal of nitric oxide (NO). *Opt. Express* **24**, 10205–10212 (2016)
6. Y. Ye et al., Theoretical and experimental investigation of highly photocatalytic performance of CuInZnS nanoporous structure for removing the NO gas. *J. Catal.* **357**, 100–107 (2018)
7. J. Liu et al., Metal-free efficient photocatalyst for stable visible water splitting via a two-electron pathway. *Science* **347**(6225), 970–974 (2015)
8. Y.-K. Peng, S.C.E. Tsan, Facet-dependent photocatalysis of nanosize semiconductive metal oxides and progress of their characterization. *Nano Today* **18**, 15–34 (2018)
9. L. Li et al., Sulfur-doped covalent triazine-based frameworks for enhanced photocatalytic hydrogen evolution from water under visible light. *J. Mater. Chem. A* **4**(32), 12402–12406 (2016)
10. A. Kudo, Y. Misek, Heterogeneous photocatalyst materials for water splitting. *Chem. Soc. Rev.* **38**(1), 253–278 (2009)
11. X. Dong, F.X. Cheng, Recent development in exfoliated two-dimensional g-C₃N₄ nanosheets for photocatalytic applications. *J. Mater. Chem. A* **3**(47), 23642–23652 (2015)
12. L. Jiang et al., Doping of graphitic carbon nitride for photocatalysis: a review. *Appl. Catal.* **217**, 388–406 (2017)
13. P. Xu et al., Use of iron oxide nanomaterials in wastewater treatment: a review. *Sci. Total Environ.* **424**, 1–10 (2012)
14. J. Liu et al., Self-assembling TiO₂ nanorods on large graphene oxide sheets at a two-phase interface and their anti-

- recombination in photocatalytic applications. *Adv. Funct. Mater.* **20**(23), 4175–4181 (2010)
15. D.-N. Bui et al., Relationship between the electrochemical behavior of multiwalled carbon nanotubes (MWNTs) loaded with CuO and the photocatalytic activity of Eosin Y-MWNTs-CuO system. *Appl. Surf. Sci.* **266**, 288–293 (2013)
 16. J. Tian et al., Recent progress in design, synthesis, and applications of one-dimensional TiO₂ nanostructured surface heterostructures: a review. *Chem. Soc. Rev.* **43**(20), 6920–6937 (2014)
 17. Y. Wang et al., Polymeric graphitic carbon nitride as a heterogenous organocatalyst: from photochemistry to multi-purpose catalysis to sustainable chemistry. *Angew. Chem. Int. Ed.* **51**(1), 68–89 (2012)
 18. J.L. White et al., Light-driven heterogenous reduction of carbon dioxide: photocatalysts and photoelectrodes. *Chem. Rev.* **115**(23), 12888–12935 (2015)
 19. C. Wang et al., Recent progress in visible light photocatalytic conversion of carbon dioxide. *J. Mater. Chem. A.* **7**(3), 865–887 (2019)
 20. A.S. Al-Hussaini et al., New semiconducting core-shell nanocomposites. *Compos Interface* **27**(4), 385–399 (2020)
 21. Z. Li et al., Design of highly stable and selective core/yolk-shell nanocatalysts-A review. *Appl Catal B-Environ* **188**, 324–341 (2016)
 22. J. Wang et al., Exceptional photocatalytic activities for CO₂ conversion on Al-O bridged g-C₃N₄/α-Fe₂O₃ Z-scheme nanocomposites and mechanism insight with isotopes. *Appl. Catal. B* **221**, 459–466 (2018)
 23. B. Sun et al., Magnetic Fe₂O₃/mesoporous black TiO₂ hollow sphere heterojunctions with wide-spectrum response and magnetic separation. *Appl. Catal. B* **221**, 235–242 (2018)
 24. P. George et al., All-optical nanoscale heating and thermometry with resonant dielectric nanoparticles for controllable drug release in living cells. *Laser Photonics Rev.* **14**(3), 1900082 (2020)
 25. L.K. Li et al., Optical fiber optofluidic bio-chemical sensors: a review. *Laser Photonics Rev.* **15**(7), 2000526 (2021)
 26. N. Wang et al., Rational design and synthesis of SnO₂ encapsulated alpha-Fe₂O₃ nanocubes as a robust and stable photo-fenton catalyst. *Appl. Catal. B* **210**, 23–33 (2017)
 27. M. Mishra, D.-M. Chun, α-Fe₂O₃ as a photocatalytic material: a review. *Appl. Catal. A Gen.* **498**, 126–141 (2015)
 28. K.S. Ranjith et al., Alignment, morphology and defect control of vertically aligned ZnO nanorod array: competition between “Surfactant” and “Stabilizer” roles of the amine species and its photocatalytic properties. *Cryst. Growth Des.* **14**(6), 2873–2879 (2014)
 29. Z.W. Zhang et al., A spontaneous dissolution approach to carbon coated TiO₂ hollow composite spheres with enhanced visible photocatalytic performance. *Appl. Surf. Sci.* **286**, 344–350 (2013)
 30. S. Shanmugam et al., Synthesis and characterization of TiO₂@C core-shell composite nanoparticles and evaluation of their photocatalytic activities. *Chem. Mater.* **18**(9), 2275–2282 (2006)
 31. J. Guo et al., Interdispersed amorphous MnOx-carbon nanocomposites with superior electrochemical performance as lithium-storage material. *Adv Funct Mater* **22**(4), 803–811 (2012)
 32. J. Liu et al., Facile synthesis of carbon-doped mesoporous anatase TiO₂ for the enhanced visible-light driven photocatalysis. *Chem. Commun.* **50**(90), 13971–13974 (2014)
 33. D.S. Knight, W.B. White, Characterization of diamond films by Raman spectroscopy. *J. Mater Res.* **4**, 385–393 (1989)
 34. J. Lu et al., One-pot synthesis of fluorescent carbon nanoribbons, nanoparticles, and graphene by the exfoliation of graphite in ionic liquids. *ACS Nano* **3**(8), 2367–2375 (2009)
 35. M.S. Dresselhaus et al., Perspectives on carbon nanotubes and graphene Raman spectroscopy. *Nano Lett.* **10**(3), 751–758 (2010)
 36. W. Zhen et al., The enhancement of CdS photocatalytic activity for water splitting via anti-photocorrosion by coating Ni₂P shell and removing nascent formed oxygen with artificial gill. *Appl. Catal. B* **221**, 1243–1257 (2018)
 37. P. Wang et al., Shell thickness engineering significantly boosts the photocatalytic H₂ evolution efficiency of CdS/CdSe core/shell quantum dots. *ACS Appl. Mater. Interfaces* **9**(41), 35712–35720 (2017)
 38. B. Cheng et al., Effects of interface States on photoexcited carriers in ZnO/Zn₂SnO₄ type-ii radial heterostructure nanowires. *ACS Appl. Mater. Interfaces* **6**(6), 4057–4062 (2014)
 39. S.C. Rai et al., Piezo-phototronic effect enhanced UV/Visible photodetector based on fully wide band gap type-ii ZnO/ZnS Core/Shell nanowire array. *ACS Nano* **9**(6), 6419–6427 (2015)
 40. M. Kim et al., Efficient visible light-induced H₂ production by Au@CdS/TiO₂ nanofibers: synergistic effect of core-shell structured Au@CdS and densely packed TiO₂ nanoparticles. *Appl. Catal. B* **166**, 423–431 (2015)
 41. C.Z. Luo et al., Preparation of 3D reticulated ZnO/CNF/NiO heteroarchitecture for high-performance photocatalysis. *Appl. Catal. B* **116**, 217–223 (2015)
 42. K. Zhang et al., Nanoconfined Nickel@Carbon core-shell cocatalyst promoting highly efficient visible-light photocatalytic H₂ production. *Small* **14**(18), 1801705 (2018)

43. X. Lü et al., A general preparation strategy for hybrid TiO₂ hierarchical spheres and their enhanced solar energy utilization efficiency. *Adv. Mater.* **22**(33), 3719–3722 (2010)
44. Y. Zhuang et al., Template free preparation of TiO₂/C core-shell hollow sphere for high performance photocatalysis. *J. Alloy. Compd.* **662**, 84–88 (2016)
45. Y. Guo et al., Synthesis of magnetic core-shell carbon dot@MFe₂O₄ (M= Mn, Zn and Cu) hybrid materials and their catalytic properties. *Mater. Chem. A* **4**(11), 4044–4055 (2016)
46. Y. Niu et al., Structures and photocatalytic activity of α -Fe₂O₃@TiO₂ core-shell nanoparticles. *Solid State Commun.* **345**, 114683 (2022)
47. Q. Tian et al., Tube-like ternary α -Fe₂O₃@SnO₂@Cu₂O sandwich heterostructures: synthesis and enhanced photocatalytic properties. *ACS Appl. Mater. Interfaces.* **6**(15), 13088–13097 (2014)
48. J. Yu et al., Photogenerated electron reservoir in hetero-p-n CuO-ZnO nanocomposite device for visible-light-driven photocatalytic reduction of aqueous Cr (VI). *J. Mater. Chem. A* **3**(3), 1199–1207 (2015)
49. N. Li et al., Precisely controlled fabrication of magnetic 3D Fe₂O₃@ZnO core-shell photocatalyst with enhanced activity: ciprofloxacin degradation and mechanism insight. *Chem. Eng. J.* **308**, 377–3853 (2017)
50. C. Wang et al., Controlled formation of TiO₂/MoS₂ core-shell heterostructures with enhanced visible-light photocatalytic activities. *Part. Part. Syst. Character.* **33**(4), 221–227 (2016)
51. S. Adhikari et al., Construction of heterojunction photoelectrode via atomic layer deposition of Fe₂O₃ on Bi₂WO₆ for highly efficient photoelectrochemical sensing and degradation of tetracycline. *Appl. Catal. B: Environ.* **24**, 11–24 (2019)
52. T. Guo et al., A novel α -Fe₂O₃@g-C₃N₄ catalyst: Synthesis derived from Fe-based MOF and its superior photo-Fenton performance. *Appl. Surf. Sci.* **469**, 331–339 (2019)
53. L. Zhu et al., Hierarchical ZnO decorated with CeO₂ nanoparticles as the direct Z-Scheme heterojunction for enhanced photocatalytic activity. *ACS Appl. Mater. Interfaces* **10**(46), 39679–396879 (2018)
54. Y. He et al., Remarkably enhanced visible-light photocatalytic hydrogen evolution and antibiotic degradation over g-C₃N₄ nanosheets decorated by using nickel phosphide and gold nanoparticles as cocatalysts. *Appl. Surf. Sci.* **517**, 146187 (2020)
55. X. Liu et al., Efficient Fe₃O₄-C₃N₄-Ag₂MoO₄ ternary photocatalyst: synthesis, outstanding light harvesting, and superior hydroxyl radical productivity for boosted photocatalytic performance. *Appl. Catal. A* **568**, 54–63 (2018)
56. H. Huang et al., Efficient activation of persulfate by a magnetic recyclable rape straw biochar catalyst for the degradation of tetracycline hydrochloride in water. *Sci. Total Environ.* **758**, 143957 (2021)
57. T. Guo et al., Efficient persulfate activation by hematite nanocrystals for degradation of organic pollutants under visible light irradiation: Facet-dependent catalytic performance and degradation mechanism. *Appl. Catal. B: Environ.* **286**, 119883 (2021)

Publisher's Note Springer Nature remains neutral with regard to jurisdictional claims in published maps and institutional affiliations.

Springer Nature or its licensor holds exclusive rights to this article under a publishing agreement with the author(s) or other rightsholder(s); author self-archiving of the accepted manuscript version of this article is solely governed by the terms of such publishing agreement and applicable law.